中国激光

激光功率对双激光粉末床熔融GH3536合金搭接区组织和性能的影响

沈沐宇，谢寅，李继康，蔡超，滕庆**，魏青松*

华中科技大学材料科学与工程学院，材料成形与模具技术国家重点实验室，湖北 武汉 430074

摘要 多激光粉末床熔融(ML-PBF)采用多束激光并行加工，是提高制造效率和大尺寸零件整体化增材制造的有效方法。但不同的激光束实际工作时参数难以保持一致，特别是激光功率会存在偏差，其中多激光搭接区最为关键。笔者通过设置4组差值为10、20、30、40 W的激光功率组合，探究了激光功率对ML-PBF制备的GH3536镍基高温合金搭接区组织和性能的影响。结果表明：成形试样的致密度最高可达99.6%，但搭接激光功率增大不仅会导致致密度降低至99.3%，孔隙率超过0.08%，还会导致γ相的衍射峰向大角度偏移，晶格常数降低。同时，随着搭接激光功率增大，搭接区内的晶粒尺寸由14.57 μm增大至17.23 μm，大角度晶界占比由36.66%上升至55.91%。搭接区内残余应力随着搭接激光功率的增大而先降低后升高，在激光功率相差30 W时降至最低值43.8 MPa。搭接区硬度随着搭接激光功率的增大而降低，由297.3 HV3降低至291.1 HV3。4组激光功率组合下制备的试样的极限抗拉强度在792.9～830.9 MPa范围内，当激光功率相差10 W时强度达到最高值，延伸率为23.7%。增大搭接激光功率会降低ML-PBF的熔凝稳定性并增大温度梯度，进而对搭接区内的微观组织、残余应力以及零件的力学性能产生影响。

关键词 激光技术；多激光粉末床熔融；增材制造；激光功率；搭接区；镍基高温合金；微观组织；残余应力；力学性能

中图分类号 TG146.1 **文献标志码** A **DOI**：10.3788/CJL230860

1 引 言

激光粉末床熔融(L-PBF)是目前加工精度最高、研究和应用最广的金属增材制造(AM)技术[1]，已被广泛应用于航空航天、生物医疗、汽车船舶等行业。随着应用的扩展，单激光束成形已难以满足高效率和大尺寸零件整体制造的需求，多激光粉末床熔融(ML-PBF)成为解决上述问题的最有效方法。

与单激光束相比，ML-PBF的搭接区存在激光重熔过程，直接影响零件内部的应力场和温度场。Promoppatum[2]研究发现双激光L-PBF成形Ti6Al4V可将冷却速度和残余应力分别降低70%和30%，搭接区第一次激光扫描决定了应力的各向异性，而第二次激光扫描则影响冷却速率和残余应力。Zhang等[3]使用有限元模拟研究了ML-PBF成形Ti6Al4V的最佳扫描策略，发现激光束数量的增加有助于降低残余应力，两束激光间隔扫描搭接区可以减小能量集中从而产生较小的温度梯度。Heeling等[4]研究双激光L-PBF成形316L不锈钢时发现增大搭接区内第二束激光的光斑直径可以提高熔池附近温度场的均匀性，改善熔池润湿性，进而提高零件的致密度。ML-PBF搭接区较其他区域经历了更多次数的激光扫描，产生了更多的热积累，进而影响内部组织和零件性能。Li等[5]发现增加激光束数量降低了Ti-6.5Al-2Zr-Mo-V合金中针状马氏体α′的粗化速率，导致硬度降低。本课题组的谢寅等[6]对比了单激光、双激光和四激光L-PBF成形GH3536合金试样，发现增加激光重熔次数不仅会使晶粒择优生长更加显著、织构指数升高，还会使大角度晶界比例降低，导致断裂延伸率降低。Zhang等[7]比较了单激光和双激光L-PBF成形AlSi10Mg合金，发现双激光扫描下的熔池宽度和深度均大于单激光扫描，且搭接区边界生成了小孔，导致试样的抗拉强度和延伸率降低。除此之外，搭接区的激光搭接率和搭接宽度也会影响成形质量。Chen等[8]经模拟预测和实验验证后指出，在ML-PBF搭接区内，激光扫描重叠率在25%～50%时可有效降低搭接区内的温度梯度，促进残余应力释放。本课题组的谢寅等[9]发现，搭接区宽度在150 μm时ML-PBF成形

收稿日期：2023-05-25；**修回日期**：2023-06-30；**录用日期**：2023-07-18；**网络首发日期**：2023-07-30

基金项目：国家自然科学基金(52201040，52275333)、中国博士后科学基金项目(2021M701291)、湖北省科技厅2020省重点研发计划(2020BAB049)、中国航空制造技术研究院稳定支持项目(KZ571801)

通信作者：*wqs_xn@163.com；**tengqing@hust.edu.cn

Hastelloy X合金具备最优的综合性能。

综上所述，ML-PBF搭接区内激光扫描策略以及搭接尺寸特征均会对搭接性能造成直接影响。现有ML-PBF研究大多采用相同的激光功率，但在实际工作中即使设置了相同的工作参数，激光功率也会有所偏差。

ML-PBF需要多套能量和扫描系统，包含激光器以及振镜、场镜等光学器件。激光器泵浦源将电能转换成泵浦光，泵浦光经增益介质及谐振腔放大后形成激光输出，其功率可能存在偏差，工作时长不同还会出现不同程度的功率衰减；此外，激光束经光路传输也会产生不同的能量损耗和聚焦效果，难以保证每束激光扫描时具有相同的激光功率[10-11]。为此，笔者以ML-PBF成形GH3536镍基高温合金为例，设置不同的激光功率差值，研究其对搭接区内冶金缺陷、组织、残余应力特征以及零件力学性能的影响，分析激光功率对搭接性能影响的原因。本研究为ML-PBF成形高性能大尺寸镍基高温合金零件奠定了理论与技术基础。

2　材料与方法

2.1　实验材料

选用宁波众远新材料科技有限公司制备的气雾化GH3536镍基高温合金粉末，其元素名义组成为Cr（21.80%，质量分数，下同）、Fe（17.43%）、Mo（9.41%）、Co（2.11%）、W（0.63%）、C（0.07%）、Ni（Bal.）。粉末的扫描电镜（SEM）形貌和粒径测试结果如图1所示，粒径为11.2～66.9 μm，中值粒径为34.7 μm。由图1（a）可知存在少量卫星粉，大部分粉末粒径均匀，适合用于L-PBF成形。

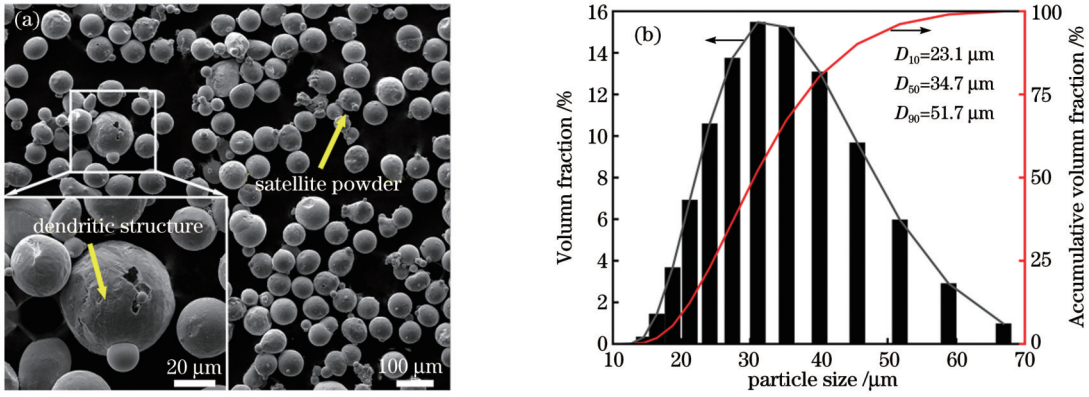

图1　GH3536合金粉末的形貌和粒径。（a）粉末的SEM形貌图；（b）粒径分布

Fig. 1　Morphology and particle size of GH3536 alloy powder. (a) SEM morphology; (b) particle size distribution

2.2　ML-PBF成形工艺

采用课题组自研L-PBF设备完成成形实验。成形台面尺寸为150 mm×150 mm，成形设备配备功率为500 W的IPG YLR-500-WC连续光纤激光器。成形腔内通入氩气形成保护气氛，腔内氧气的体积分数保持在0.02%以下。成形前，GH3536粉末置于烘箱中并在90 ℃下干燥10 h。

选用本课题组优化后的工艺参数[9,12]：铺粉层厚40 μm，扫描速度600 mm/s，扫描间距100 μm，相邻层扫描夹角67°，搭接区宽度150 μm。设计并成形了4组不同激光功率下的搭接试样，成形长条的尺寸为60 mm×12 mm×8 mm，搭接策略如图2所示。每组试样先使用前期获得的最优激光功率（240 W）完成试样一侧的扫描，然后分别使用250、260、270、280 W激光功率完成另一侧的扫描。其中，功率固定不变的激光称为“首次扫描激光”，功率变化的激光称为“搭接激光”，其功率称为“搭接激光功率”，两次激光扫描路径的重叠处称为“搭接区”。

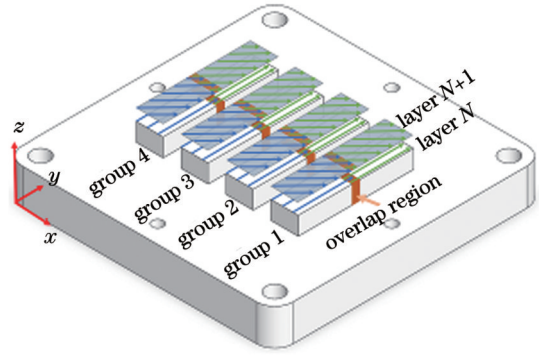

图2　不同搭接激光功率下ML-PBF成形GH3536合金的扫描策略

Fig. 2　Scanning strategy of GH3536 alloy specimens formed by ML-PBF with different laser powers

2.3　组织表征与性能检测

从4组试样搭接区附近采用线切割分别加工出3个尺寸为4 mm×4 mm×5 mm的测试样件。致密度采用阿基米德排水法测量。试样经400～3000目砂纸研磨及机械抛光后，在光学显微镜（Leica DM750M）下观察其内部的孔隙和裂纹，并使用Image J软件统计孔隙率。用A2电解液腐蚀试样后，利用扫描电镜（JEOL JSM 7600F）观察显微组织，利用场发射扫描电子显微镜（FEI Quanta 650 FEG）完成电子背散射衍射（EBSD）表征。利用X射线衍射仪（PANalytical

X’Pert3 powder)进行物相分析，并在73°～76°衍射角范围内扫描(220)衍射峰，完成残余应力测试[13-14]。利用维氏硬度计(Wilson 430SVD)测量硬度，加载载荷为29.4 N。参照ASTM E8M标准制备拉伸试样，在材料高温持久性能试验机(Shimadzu AG-IC 100KN)上以1 mm/min的拉伸速度完成室温拉伸测试。

3 结果与讨论

3.1 孔隙缺陷

图3为4组试样的致密度和孔隙率测试结果以及孔隙的显微形貌。致密度随搭接激光功率增大呈下降趋势，从99.6%逐渐降低至99.3%；孔隙率则随着搭接激光功率增大而升高，搭接激光功率最大时孔隙率超过了0.08%。搭接区内激光重复扫描可以消除残存的未熔粉末，增大搭接激光功率可以提高金属熔体的流动性，但不断增大的搭接激光功率会导致更高的能量输入，使得熔池中的金属液滴飞溅，加剧了搭接区的不稳定程度[15-16]。由图3(b)～(e)可以看出第一组和第二组试样中的孔隙较少，孔隙形貌以微小圆孔为主，该类孔隙多为熔池中未能及时逃逸的保护气所致[17]。当搭接激光功率最大时，孔隙尺寸明显增大，并变成不规则的形状。

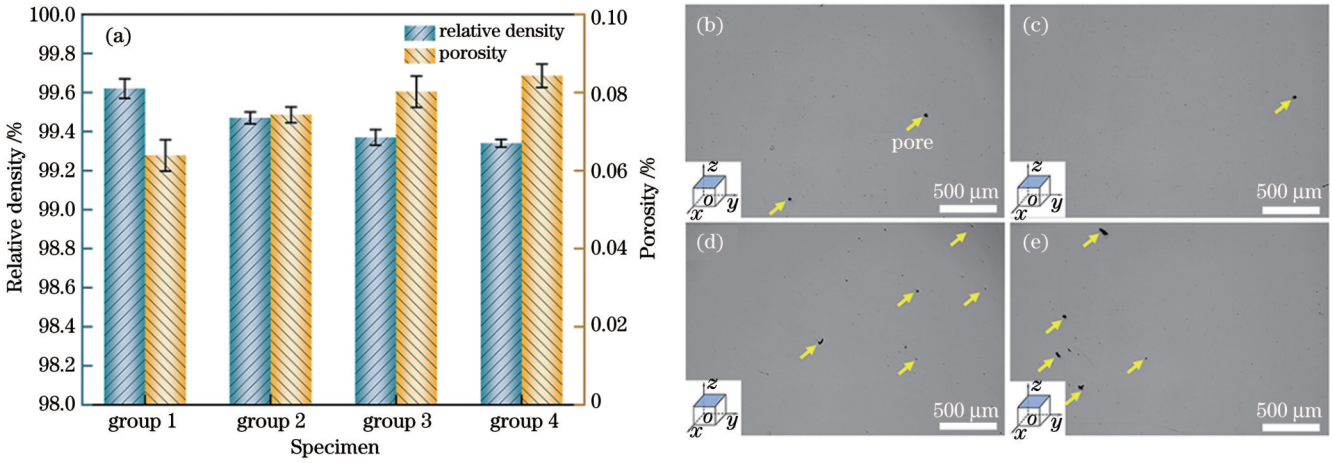

图3 致密度和孔隙率结果。(a)致密度和孔隙率；(b)～(e)第一到第四组试样搭接区孔隙的显微形貌

Fig. 3 Measured relative density and porosity. (a) Relative density and porosity; (b)-(e) micro-pores morphology in the overlap region of specimens of groups 1, 2, 3 and 4

3.2 相分析

为了探究不同组试样物相间的差异，对4组试样进行了XRD测试。图4所示的XRD测试结果表明，4组试样搭接区均由面心立方结构的γ相组成，4组试样的(200)衍射峰均向大角度方向偏移。这源于ML-PBF中的热积聚效应，搭接激光功率越大，偏移量越大[5]。第一到第四组试样的(200)衍射峰的半峰全宽分别为0.69°、0.51°、0.33°和0.27°。根据Scherrer公式，晶粒尺寸随着半峰全宽的减小而增大，故搭接区内晶粒尺寸随着搭接激光功率的增大而变大。用布拉格衍射方程计算4组试样的晶格常数，计算结果如表1所示。晶格常数随着搭接激光功率增大而降低，其原因在于增大搭接激光功率提高了搭接区的温度，为元素

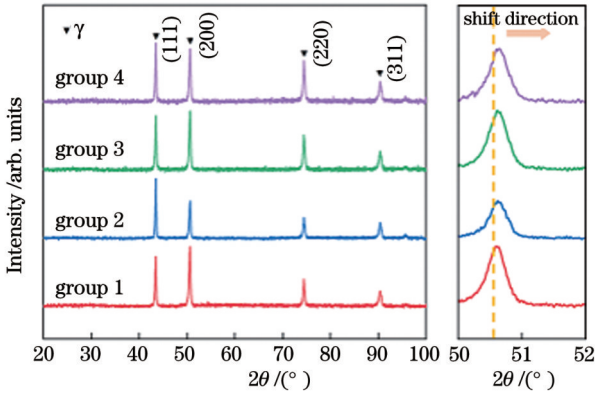

图4 4组试样搭接区的XRD测试结果

Fig. 4 XRD results of four groups of specimens in the overlap region

表1 4组试样中γ相晶格常数的计算结果

Table 1 Calculated lattice constant of γ phase in four groups of specimens

Group	Wavelength λ_{Cu} /nm	Diffraction angle 2θ /(°)	Interplanar crystal spacing /nm	Lattice constant /Å
Group 1	0.15406	50.58	0.09015	0.18031
Group 2	0.15406	50.62	0.09009	0.18018
Group 3	0.15406	50.66	0.09002	0.18005
Group 4	0.15406	50.68	0.08999	0.17998

扩散提供了有利环境，促进了合金的脱溶分解，从而提高了合金的脱溶度[18]。

3.3　显微形貌及组织分析

图 5 为 4 组试样搭接区上表面熔化道形貌。当搭接激光功率较小时，搭接区表面相对平整，如图 5(a)所示；随着搭接激光功率增大，搭接区表面出现凸起“褶皱”，如图 5(b)～(d)所示。这是因为激光功率增大促进了熔池内液态金属的流动，当熔融金属接触到已凝固组织时温度急剧下降并迅速凝固，保留着与非搭接区碰撞时的形貌，这也被称为“重叠边界效应”[19]。如图 5(d)所示，在最大搭接激光功率试样中观察到了部分未熔粉末，这是激光功率过大产生的粉末飞溅所致[20]。搭接激光功率增大后，激光与金属粉末相互作用加剧，熔池上方形成的金属蒸气对熔池前沿和侧壁产生反冲压力，导致熔池周围的粉末颗粒脱离粉床，扬起的粉末颗粒在重力作用下落在成形表面上形成粉末飞溅。

图 6 为 4 组试样沿成形方向搭接区内晶粒的形貌，即使 4 组试样的搭接激光功率存在差异，但仍可

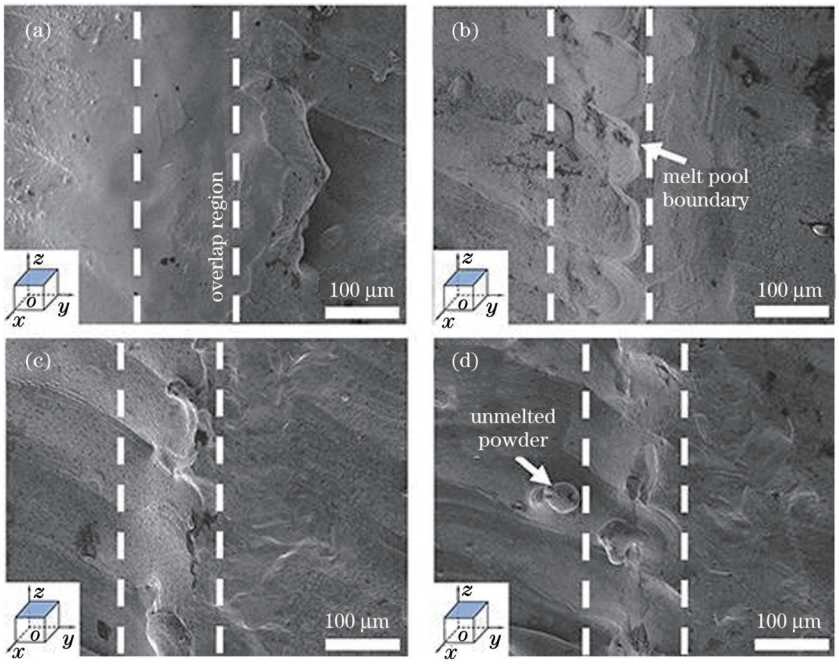

图 5　搭接区上表面的 SEM 形貌。(a)第一组；(b)第二组；(c)第三组；(d)第四组

Fig. 5　Scanning electron micrographs of the upper surface of the overlap region. (a) Group 1; (b) group 2; (c) group 3; (d) group 4

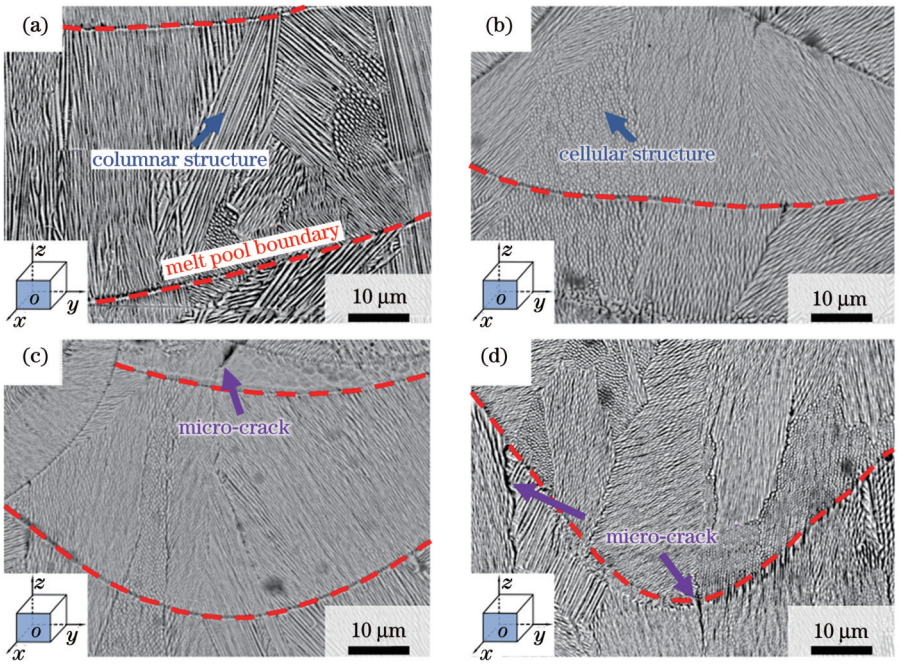

图 6　沿成形方向搭接区晶粒的 SEM 形貌。(a)第一组；(b)第二组；(c)第三组；(d)第四组

Fig. 6　Scanning electron micrographs of overlap region grains in the building direction. (a) Group 1; (b) group 2; (c) group 3; (d) group 4

清晰地观察到L-PBF特有的“鱼鳞状”熔池形貌。激光功率决定了激光的能量密度，增大搭接激光功率后，激光对材料的穿透力增强，搭接区熔池底部边界的弯曲程度随之增大。搭接区历经两次激光扫描后熔池内部组织仍保留L-PBF特征，即组织由柱状结构和胞状结构共同组成[21]。进一步观察第三组和第四组试样可以发现搭接激光功率相差30 W时，熔池边界附近易萌发微裂纹。这是由于高密度的热量输入无法在极短的凝固过程中完全排出，较高温度梯度导致相邻熔池的结合界面边缘产生了裂纹[22-23]。

图7为4组试样搭接区附近沿成形方向截面的EBSD测试结果。4组试样搭接区两侧晶粒的尺寸发生了变化，功率较高的搭接激光扫描一侧[图7(a)、(d)、(g)、(j)右侧]较首次激光扫描一侧[图7(a)、(d)、(g)、(j)左侧]的晶粒明显更加粗大。搭接区

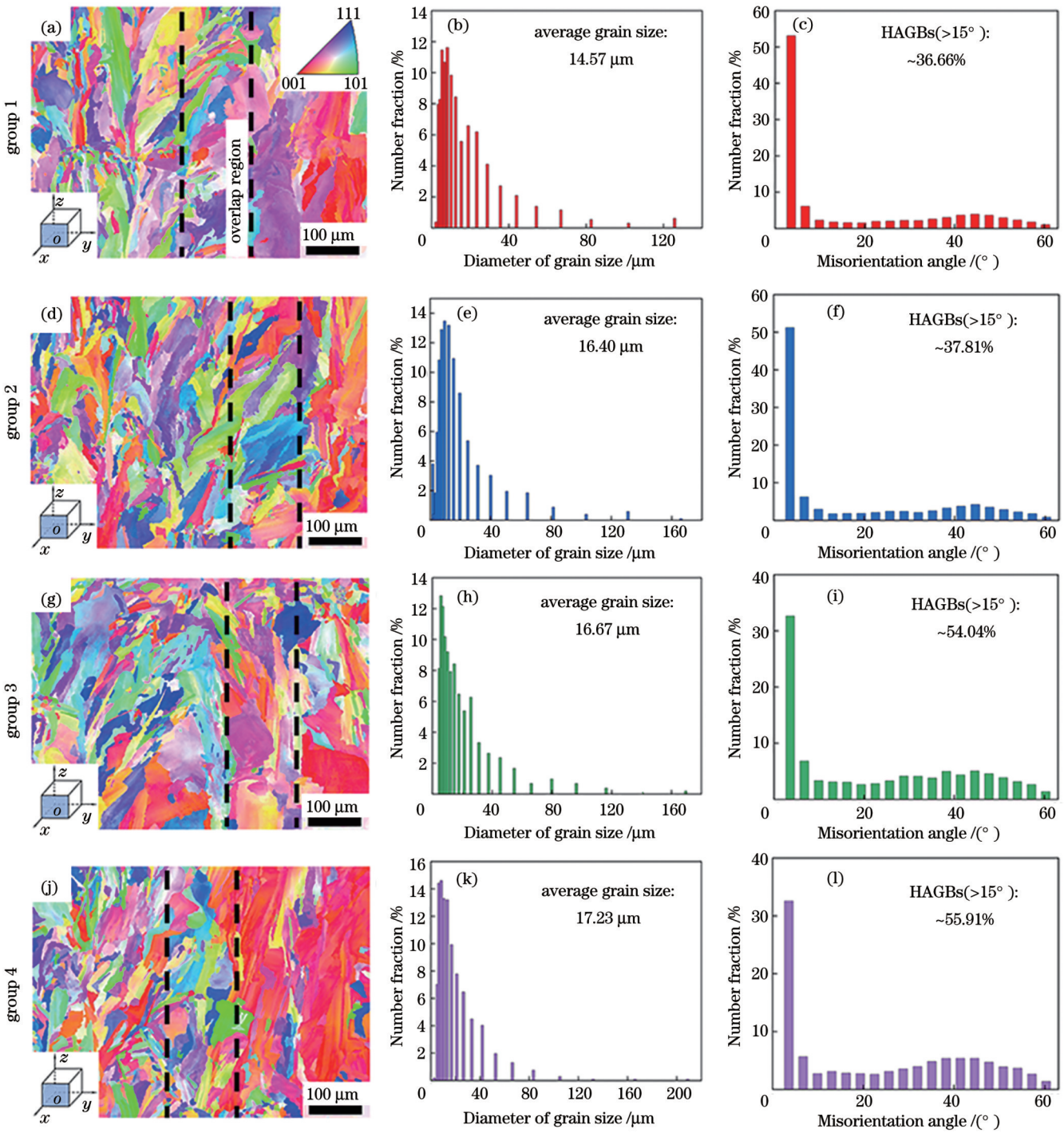

图7　沿成形方向搭接区的EBSD结果。(a)(d)(g)(j)反极图；(b)(e)(h)(k)晶粒尺寸统计结果；(c)(f)(i)(l)晶粒位向差统计

Fig. 7　EBSD results of overlap region in the building direction. (a)(d)(g)(j) Inverse pole figures (IPFs); (b)(e)(h)(k) grain size statistics; (c)(f)(i)(l) misorientation angle statistics

内晶粒尺寸不均匀，但均沿〈111〉方向择优生长。图 7(b)、(e)、(h)、(k)为搭接区内晶粒尺寸的统计结果。第一组试样的晶粒尺寸最小，仅为 14.57 μm；当搭接激光功率最高时，晶粒尺寸达到了 17.23 μm。这是因为高功率激光引起的高温提高了晶界移动能力，增大了原子扩散能力，从而加速了晶粒的生长速度，促进晶粒长大。根据 Hall-Petch 公式，减小金属材料的晶粒尺寸可以提高其屈服强度。在多晶材料中，晶界的自由能远高于晶粒内部的自由能，晶界是阻碍位错运动的势垒。金属材料发生塑性变形时，较小尺寸的晶粒能够增大晶界面积并降低应力集中，进而提高材料强度[24]。搭接激光功率的增大会大幅提升搭接区内大角度晶界（HAGBs）的比例。图 7(c)、(f)、(i)、(l)给出了 4 组试样搭接区晶粒间的位向差统计结果，可见：随着搭接激光功率差值由 20 W 增大到 30 W，搭接区内大角度晶界所占比例由 37.81% 上升至 54.04%，激光功率差值保持在 20 W 内可获得较高比例的小角度晶界。根据式(1)所示的位错理论，晶界能(γ_{gb})取决于位错角(θ)，故大角度晶界处往往蕴含的晶界能较高[25]。液膜形成的驱动力由晶间过冷度主导，如式(2)所示。在冷却过程中，当晶界能 γ_{gb} 大于固/液界面能 γ_{sl} 时，晶间存在液膜，随后液膜在内应力或凝固收缩作用力下开裂形成裂纹[26]。

$$\gamma_{gb}=\frac{Gb\theta}{4\pi(1+v)}\left(1-\ln\frac{\theta}{\theta_m}\right), \tag{1}$$

$$\Delta T_b=\frac{\gamma_{gb}-2\gamma_{sl}}{\Delta S_f\cdot\delta}, \tag{2}$$

式中：v 为泊松比；G 为剪切模量；b 为柏氏矢量的大小；θ_m 为最大晶界能对应的角度；ΔS_f 为熔化熵；δ 为扩散界面厚度；γ_{gb} 为晶界能；γ_{sl} 为固/液界面能。

3.4　残余应力

搭接区经多次熔化与凝固后，试样的晶面间距会因残余应力导致的晶格畸变发生改变，因此笔者采用 X 射线衍射法进行了残余应力测试。首先根据每组试样在不同倾转角(ψ)下的峰位变化，利用直线拟合晶面间距(d)与倾转角正弦值的平方($\sin^2\psi$)得到斜率，该斜率与残余应力成正比，最终通过式(3)间接计算出材料内部的残余应力(σ)[27]。

$$\sigma=\frac{(d_\psi-d_n)\cdot E}{d_0\cdot\sin^2\psi\cdot(1+v)}\approx\frac{(d_\psi-d_n)\cdot E}{d_n\cdot\sin^2\psi\cdot(1+v)}, \tag{3}$$

式中：d_n、d_ψ、d_0 分别为晶面平行于应力方向、晶面与应力呈角度 ψ 以及无应力时的晶面间距；v 为泊松比；E 为弹性模量。图 8 为 4 组试样($\sin^2\psi$，d_ψ)数据点以及线性拟合结果。拟合直线的斜率随搭接激光功率的升高而先减小后增大，故试样中的残余应力先降低后升高。接下来进一步进行定量分析。设定 GH3536 镍基高温合金的弹性模量为 200 GPa，泊松比为 0.3[6]，由式(3)可以计算出 4 组试样的残余应力值分别为 130.6、68.2、43.8、99.4 MPa。随着搭接激光功率差值从 10 W 增大到 30 W，搭接区的残余应力有效降低。在激光熔融过程中，材料受到激光周期性的热作用，出现拉应力与压

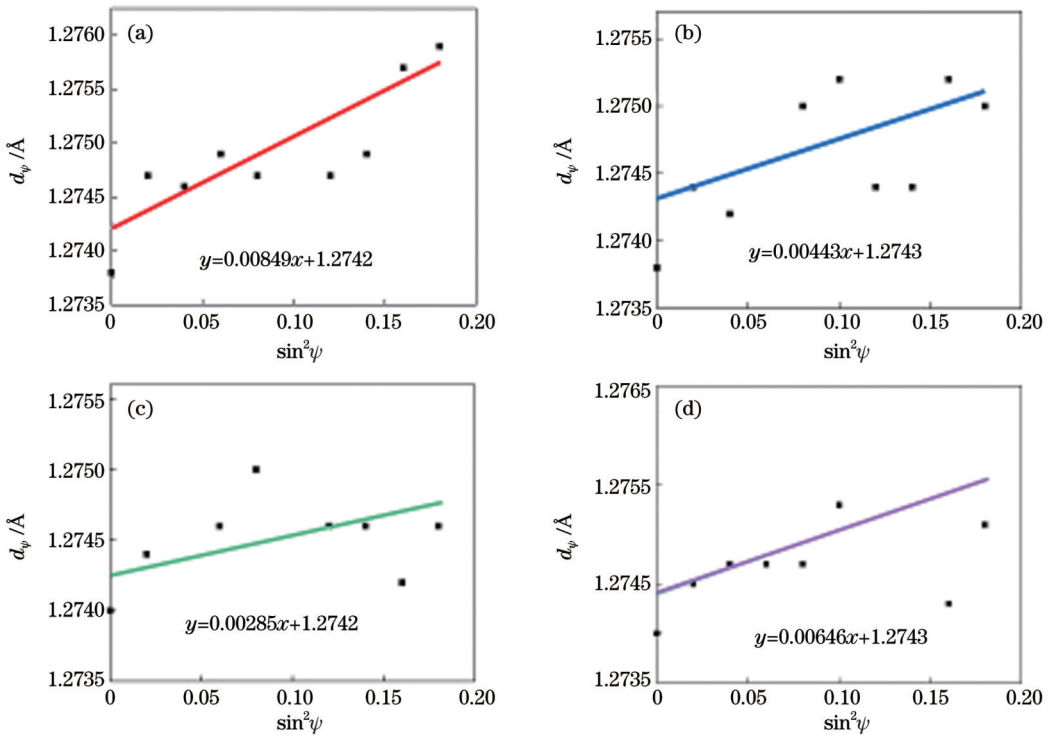

图 8　d_ψ 与 $\sin^2\psi$ 值的散点图及线性拟合。(a)第一组；(b)第二组；(c)第三组；(d)第四组

Fig. 8　Scatter plots and linear fit of d_ψ and $\sin^2\psi$. (a) Group 1; (b) group 2; (c) group 3; (d) group 4

应力的频繁转换，内部应力的作用影响了搭接区内的残余应力水平[28]。在一定范围内，搭接激光功率的升高会使材料发生塑性变形和局部弛豫，从而释放残余应力，但搭接激光功率过大则会引起更高的熔池温度梯度，造成更严重的变形，形成的应力大于释放的应力，导致残余应力增大。

3.5　力学性能

经双激光扫描后搭接区的维氏硬度变化如图 9 所示。随着搭接激光功率增大，4 组试样的硬度测试结果依次为 297.3、294.7、292.8、291.1 HV3，硬度值逐渐降低。这主要是由于 GH3536 合金中的 γ 相基体和碳化物等受激光热循环作用发生 Cr、Mo 元素脱溶，导致合金脆化、硬度值下降，而且搭接激光功率越高，硬度降低得越显著[29]。同时，激光功率的增大也导致热影响区扩大，促进晶粒生长，进而造成搭接区硬度下降。

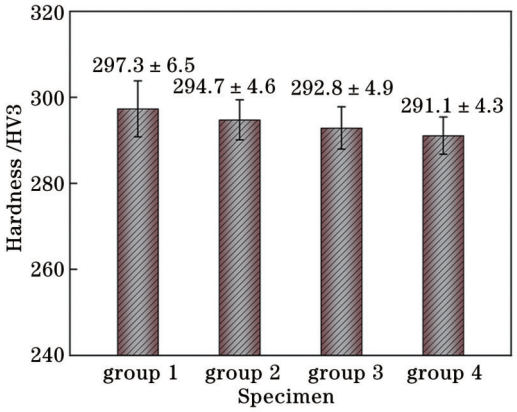

图 9　搭接区硬度统计

Fig. 9　Hardness statistics of overlap region

图 10 为 4 组试样的室温拉伸测试结果。随着搭接激光功率增大，强度和延伸率总体呈下降趋势，极限抗拉强度（UTS）最高可达 830.9 MPa，延伸率最高可达 23.7%。其主要原因是搭接激光功率增大会导致孔隙和裂纹。前三组试样的屈服强度（YS）均在 670 MPa 以上，第四组试样的屈服强度降低至 624.1 MPa，抗拉强度降至 792.9 MPa，延伸率仅为 18.7%。GH3536 合金主要通过材料内部的长、短程内应力场以及原子偏聚等障碍来阻止位错滑移，增大滑移所需的流变应力，从而起到强化合金的效果。搭接激光功率的升高提高了合金中内应力的释放程度和原子活动能力，固溶强化效果降低，因而拉伸性能下降。

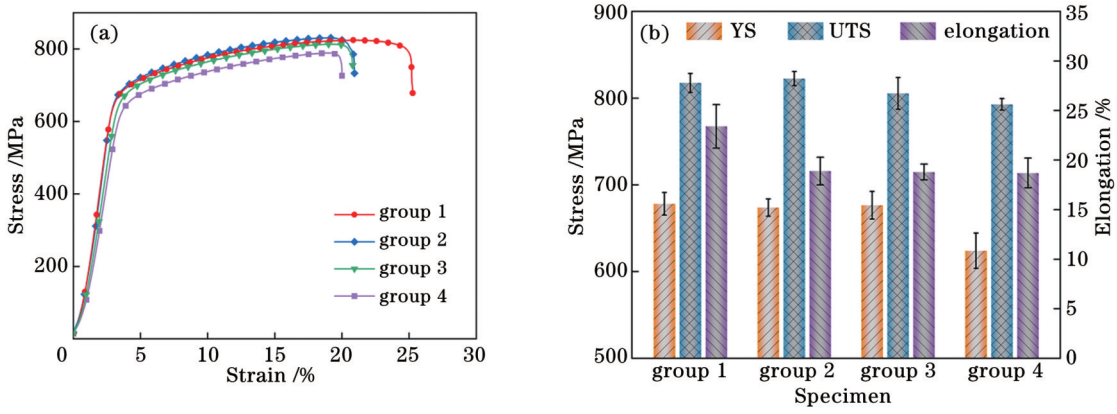

图 10　4 组试样的拉伸性能。(a)沿水平方向的应力-应变曲线图；(b)沿水平方向的屈服强度、抗拉强度及延伸率

Fig. 10　Tensile properties of four groups of specimens. (a) Horizontal stress-strain curves; (b) horizontal yield strength, tensile strength and elongation

4　结　　论

当搭接激光功率与首次扫描激光功率接近时，致密度高达 99.6%。随着搭接激光功率增大，搭接区孔隙数量增多并且孔隙尺寸变大，同时孔隙由细小球状向不规则状转变，致密度降低。

4 组试样的搭接区均由 γ 相组成。随着搭接激光功率增大，(200)衍射峰向大角度方向偏移且偏移量逐渐增大，晶格常数逐渐降低。随着搭接激光功率继续增大，搭接区表面出现凸起的“褶皱”，内部晶粒尺寸变大；当搭接激光功率增大 30 W 后，大角度晶界占比大幅上升，超过 50%，导致熔池边界萌生微裂纹。

成形过程中搭接激光功率增加不超过 30 W 时，激光重熔能有效地降低搭接区的残余应力（由 130.6 MPa 降低至 43.8 MPa）。前三组试样的屈服强度均在 670 MPa 以上，抗拉强度在 814.2～830.9 MPa 之间，延伸率最高可达 23.7%。当搭接激光功率增大 40 W 后，搭接区残余应力升至 99.4 MPa，抗拉强度降至 792.9 MPa，延伸率仅为 18.7%。

参　考　文　献

[1]　顾冬冬，张红梅，陈洪宇，等. 航空航天高性能金属材料构件激光增材制造[J]. 中国激光，2020，47(5)：0500002.
Gu D D, Zhang H M, Chen H Y, et al. Laser additive manufacturing of high-performance metallic aerospace components [J]. Chinese Journal of Lasers, 2020, 47(5): 0500002.

[2]　Promoppatum P. Dual-laser powder bed fusion additive manufacturing: computational study of the effect of process

strategies on thermal and residual stress formations[J]. The International Journal of Advanced Manufacturing Technology, 2022, 121(1): 1337-1351.

[3] Zhang W Y, Tong M M, Harrison N M. Scanning strategies effect on temperature, residual stress and deformation by multi-laser beam powder bed fusion manufacturing[J]. Additive Manufacturing, 2020, 36: 101507.

[4] Heeling T, Wegener K. The effect of multi-beam strategies on selective laser melting of stainless steel 316L[J]. Additive Manufacturing, 2018, 22: 334-342.

[5] Li S H, Yang J J, Wang Z M. Multi-laser powder bed fusion of Ti-6.5Al-2Zr-Mo-V alloy powder: defect formation mechanism and microstructural evolution[J]. Powder Technology, 2021, 384: 100-111.

[6] 谢寅, 滕庆, 沈沐宇, 等. 多激光粉床熔融成形GH3536合金搭接区域组织与性能特征研究[J]. 中国激光, 2023, 50(8): 0802303.
Xie Y, Teng Q, Shen M Y, et al. Study on microstructure and properties of overlap region of GH3536 alloy processed by multi-laser powder bed fusion[J]. Chinese Journal of Lasers, 2023, 50(8): 0802303.

[7] Zhang C C, Zhu H H, Hu Z H, et al. A comparative study on single-laser and multi-laser selective laser melting AlSi10Mg: defects, microstructure and mechanical properties[J]. Materials Science and Engineering: A, 2019, 746: 416-423.

[8] Chen C P, Yin J, Zhu H H, et al. Effect of overlap rate and pattern on residual stress in selective laser melting[J]. International Journal of Machine Tools and Manufacture, 2019, 145: 103433.

[9] Xie Y, Teng Q, Shen M Y, et al. The role of overlap region width in multi-laser powder bed fusion of Hastelloy X superalloy [J]. Virtual and Physical Prototyping, 2023, 18(1): e2142802.

[10] 王华明. 高性能大型金属构件激光增材制造: 若干材料基础问题[J]. 航空学报, 2014, 35(10): 2690-2698.
Wang H M. Materials′ fundamental issues of laser additive manufacturing for high-performance large metallic components[J]. Acta Aeronautica et Astronautica Sinica, 2014, 35(10): 2690-2698.

[11] 杨永强, 吴世彪, 张越, 等. 光纤激光器在金属增材制造中的应用进展及展望[J]. 中国激光, 2020, 47(5): 203-215.
Yang Y Q, Wu S B, Zhang Y, et al. Application progress and prospect of fiber laser in metal additive manufacturing[J]. Chinese Journal of Lasers, 2020, 47(5): 203-215.

[12] Sun S S, Teng Q, Xie Y, et al. Two-step heat treatment for laser powder bed fusion of a nickel-based superalloy with simultaneously enhanced tensile strength and ductility[J]. Additive Manufacturing, 2021, 46: 102168.

[13] Saarimaki J, Lundberg M, Moverare J J, et al. 3D residual stresses in selective laser melted hastelloy X[J]. Materials Research Proceedings, 2017, 2: 73-78.

[14] Shaji Karapuzha A, Wegener T, Krochmal M, et al. Fatigue crack growth in additively manufactured Hastelloy X: influences of crack orientation and post-fabrication treatments[J]. Materials Science and Engineering: A, 2022, 854: 143773.

[15] Slodczyk M, Ilin A, Kiedrowski T, et al. Spatter reduction by multi-beam illumination in laser powder-bed fusion[J]. Materials & Design, 2021, 212: 110206.

[16] Leung C L A, Marussi S, Atwood R C, et al. *In situ* X-ray imaging of defect and molten pool dynamics in laser additive manufacturing[J]. Nature Communications, 2018, 9: 1355.

[17] Chen T, Pang S Y, Tang Q, et al. Evaporation ripped metallurgical pore in electron beam freeform fabrication of Ti-6-Al-4-V[J]. Materials and Manufacturing Processes, 2016, 31(15): 1995-2000.

[18] 卞玉超, 彭英博, 宋凌峰, 等. 基于激光重熔优化工艺的激光选区熔化316L/IN718异质异构研究[J]. 中国激光, 2021, 48(18): 1802009.
Bian Y C, Peng Y B, Song L F, et al. Heterogeneity of 316L/IN718 formed via selective laser melting based on laser remelting optimization process[J]. Chinese Journal of Lasers, 2021, 48(18): 1802009.

[19] Li Z H, Liu W P, Liu B, et al. Difference-extent of microstructure and mechanical properties: simulating multi-laser selective melting Ti6Al4V[J]. Optics & Laser Technology, 2022, 153: 108249.

[20] Young Z A, Guo Q L, Parab N D, et al. Types of spatter and their features and formation mechanisms in laser powder bed fusion additive manufacturing process[J]. Additive Manufacturing, 2020, 36: 101438.

[21] Wei W, Xiao J C, Wang C F, et al. Hierarchical microstructure and enhanced mechanical properties of SLM-fabricated GH5188 Co-superalloy[J]. Materials Science and Engineering: A, 2022, 831: 142276.

[22] 刘鹏良, 孙文磊, 黄勇. 温度梯度对激光熔覆层裂纹产生的影响[J]. 激光技术, 2019, 43(3): 392-396.
Liu P L, Sun W L, Huang Y. Effect of temperature gradient on cracks in laser cladding layer[J]. Laser Technology, 2019, 43(3): 392-396.

[23] Teng Q, Li S, Wei Q S, et al. Investigation on the influence of heat treatment on Inconel 718 fabricated by selective laser melting: microstructure and high temperature tensile property[J]. Journal of Manufacturing Processes, 2021, 61: 35-45.

[24] Lee J U, Kim Y K, Seo S M, et al. Effects of hot isostatic pressing treatment on the microstructure and tensile properties of Ni-based superalloy CM247LC manufactured by selective laser melting[J]. Materials Science and Engineering: A, 2022, 841: 143083.

[25] Chen Y, Lu F G, Zhang K, et al. Dendritic microstructure and hot cracking of laser additive manufactured Inconel 718 under improved base cooling[J]. Journal of Alloys and Compounds, 2016, 670: 312-321.

[26] Rappaz M, Jacot A, Boettinger W J. Last-stage solidification of alloys: theoretical model of dendrite-arm and grain coalescence[J]. Metallurgical and Materials Transactions A, 2003, 34(3): 467-479.

[27] Fitzpatrick M, Fry A, Holdway P, et al. Determination of residual stresses by X-ray diffraction[J]. Measurement Good Practice Guide, 2002, 52: 12-30.

[28] Li C, Liu Z Y, Fang X Y, et al. Residual stress in metal additive manufacturing[J]. Procedia CIRP, 2018, 71: 348-353.

[29] Qiao G W, Zhang B, Bai Q, et al. Effect of heat treatment on microstructure and residual stress of GH3536 superalloy fabricated by selective laser melting[J]. Journal of Materials Engineering and Performance, 2021, 30(12): 8892-8900.

Influence of Laser Power on Microstructure and Properties of Overlap Region in Dual-Laser Powder Bed Fusion of GH3536 Superalloy

Shen Muyu, Xie Yin, Li Jikang, Cai Chao, Teng Qing**, Wei Qingsong*

State Key Laboratory of Materials Processing and Die & Mould Technology, School of Materials Science and Technology, Huazhong University of Science and Technology, Wuhan 430074, *Hubei, China*

Abstract

Objective Multi-laser powder bed fusion (ML-PBF) has been widely used in the aerospace, biomedical, and automotive marine industries owing to its high efficiency. ML-PBF equipment consists of multiple energy and scanning systems, such as lasers, galvanometers, *F*-theta lenses, and other optics. Because the pump source is converted into pump light and then amplified by the gain medium and resonant cavity to form a laser output, there may be deviations in the laser power among multiple lasers. Meanwhile, the power degradation after continuous operation differs. Transmission of a laser beam through an optical path causes different energy losses. Therefore, it is difficult to ensure that each laser beam has the same power during the ML-PBF process. Therefore, this study focuses on the effect of power deviations on the forming quality of a GH3536 nickel-based superalloy using ML-PBF. The metallurgical defects in the overlap region, microstructure, and residual stress characteristics are analyzed by setting up different laser power groups. This study aims to lay a theoretical and technical foundation for ML-PBF to form high-performance large-sized parts.

Methods Self-developing ML-PBF equipment was used in this study, and gas-atomized GH3536 nickel-based superalloy powder was measured and found to have a size distribution of 11.2–66.9 μm. Each group of specimens was first scanned on one side using the optimal laser power (240 W), and the other side was scanned at 250, 260, 270, and 280 W. The width of the overlap regions of the four specimen groups was 150 μm. First, three specimens with dimensions of 4 mm×4 mm×5 mm were machined from the vicinity of the overlap regions of each specimen using wire electrical discharge machining. The relative densities of the specimens were measured using the Archimedes' principle. After grinding with 400–3000 grit sandpaper and mechanical polishing, the internal pores and cracks were observed using an optical microscope (Leica DM750M, Germany), and the porosity was calculated using Image J software. After etching with A2 electrolyte, the microstructure was observed using a scanning electron microscope (JEOL JSM 7600F, Japan), EBSD characterization was performed using a field emission scanning electron microscope (FEI Quanta 650 FEG, USA), physical phase analyses were conducted using an X-ray diffractometer (PANalytical X'Pert3 powder, Netherlands), and residual stress testing was performed using the (220) diffraction peaks at ten tilt angles. The hardness was measured using a Vickers hardness tester (Wilson 430SVD, USA) with a test load of 29.4 N. Tensile specimens were prepared according to ASTM E8M, and room-temperature tensile tests were performed using a high-temperature endurance tester (Shimadzu AG-IC 100KN, Japan) at a tensile speed of 1 mm/min.

Results and Discussions Increasing the power of the overlap laser power causes instability in the overlap region. The relative densities gradually decrease from 99.6% to 99.3%, and the maximum porosity exceeds 0.08%. The pore morphology shifts from tiny round holes to large irregular shapes (Fig. 3). The overlap regions of the four specimen groups consist of a face-centered cubic γ phase. Owing to the thermal accumulation effect in the ML-PBF process, the (200) diffraction peaks of the four groups of specimens shift toward a large angle (Fig. 4). Increasing the overlap laser power promotes the desolvation of the alloying elements; thus, the lattice constants of the four groups of specimens decrease sequentially (Table 1). The increased laser power promotes the fluidity of the metal liquid in the molten pool. When the molten metal contacts the solidified region, it solidifies rapidly and retains the moment of collision with the non-overlap region. Thus, convex folds appear on the surface of the overlap region and are accompanied by powder spattering at the maximum laser power (Fig. 5). Increasing the overlap laser power increases the penetration of the laser into the material. Consequently, the degree of bending at the bottom boundary of the molten pool in the lap zone increases. The internal microstructure of the molten pool in the overlap region after two laser scans retains its characteristics, which consist of both columnar and cellular structures. A higher temperature gradient leads to cracks at the edge of the bonding interface of the neighboring molten pool (Fig. 6). The high temperature induced by the high-power laser improves the movement of the grain boundaries and atomic diffusion, which accelerates the growth rate of grains and promotes the growth of grains from 14.57 to 17.23 μm. When the overlap laser power difference is increased from 20 to 30 W, the proportion of high angle grain boundaries in the overlap region increases from 37.81% to 54.04%. The laser power fluctuation is maintained within 20 W to obtain a high percentage of small-angle grain boundaries (Fig. 7). The specimens are subjected to the cyclic thermal action of the laser during the laser-melting process, which results in frequent transitions between tensile and compressive stresses. Internal stresses affect the residual stress level in the overlap region. The residual stress values of the four specimen groups are 130.6, 68.2, 43.8, and 99.4 MPa(Fig. 8). The hardness decreases with increasing overlap laser power (Fig. 9). The strength and elongation generally decrease with increasing overlap laser power. The ultimate tensile strength reaches 830.9 MPa and elongation reaches 23.7%. The increase in the overlap laser power results in porosity and cracking; the yield strength of the first three groups of specimens is above 670 MPa, and that of the fourth group decreases to

624.1 MPa (Fig. 10).

Conclusions Four groups of specimens prepared using ML-PBF have a relative density of up to 99.6%. However, when the overlap laser power is increased, the relative density decreases to 99.3%, and the porosity is greater than 0.08%. The γ-phase (200) diffraction peak shifts to a large angle, and the lattice constant decreases. Furthermore, with the increase in the overlap laser power, the grain size in the overlap region increases from 14.57 to 17.23 μm, and the percentage of high angle grain boundaries increases from 36.66% to 55.91%. The residual stress in the overlap region decreases and then increases with increasing overlap laser power. The ultimate tensile strength of the specimens prepared under the four laser power combinations ranges from 792.9 to 830.9 MPa, and the strength reaches its highest value and the elongation is 23.7% when the laser power difference is 10 W.

Key words laser technique; multi-laser powder bed fusion; additive manufacturing; laser power; overlap region; nickel-based superalloy; microstructure; residual stress; mechanical properties